Journal of Astronomical Telescopes, Instruments, and Systems

AstronomicalTelescopes.SPIEDigitalLibrary.org

Using local correlation tracking to recover solar spectral information from a slitless spectrograph

Hans T. Courrier
Charles C. Kankelborg

SPIE.

Hans T. Courrier, Charles C. Kankelborg, "Using local correlation tracking to recover solar spectral information from a slitless spectrograph," *J. Astron. Telesc. Instrum. Syst.* **4**(1), 018001 (2018), doi: 10.1117/1.JATIS.4.1.018001.

Using local correlation tracking to recover solar spectral information from a slitless spectrograph

Hans T. Courrier* **and Charles C. Kankelborg**
Montana State University, Department of Physics, Solar Group, Bozeman, Montana, United States

Abstract. The Multi-Order Solar EUV Spectrograph (MOSES) is a sounding rocket instrument that utilizes a concave spherical diffraction grating to form simultaneous images in the diffraction orders $m = 0$, $+1$, and -1. MOSES is designed to capture high-resolution cotemporal spectral and spatial information of solar features over a large two-dimensional field of view. Our goal is to estimate the Doppler shift as a function of position for every MOSES exposure. Since the instrument is designed to operate without an entrance slit, this requires disentangling overlapping spectral and spatial information in the $m = \pm 1$ images. Dispersion in these images leads to a field-dependent displacement that is proportional to Doppler shift. We identify these Doppler shift-induced displacements for the single bright emission line in the instrument passband by comparing images from each spectral order. We demonstrate the use of local correlation tracking as a means to quantify these differences between a pair of cotemporal image orders. The resulting vector displacement field is interpreted as a measurement of the Doppler shift. Since three image orders are available, we generate three Doppler maps from each exposure. These may be compared to produce an error estimate. [DOI: 10.1117/1.JATIS.4.1.018001]

Keywords: spectroscopy; extreme ultraviolet; image processing; space optics; stereoscopy; sun.

Paper 17028P received Jun. 20, 2017; accepted for publication Dec. 13, 2017; published online Jan. 12, 2018.

1 Introduction

The transition region is the portion of the solar atmosphere between the million degree corona and the much cooler chromosphere. To understand the underlying physical mechanisms that result in this temperature disparity, it is necessary to characterize the solar atmosphere in the spatial, temporal, and spectral domains. Spectrographic observations point to a number of mechanisms by which the corona may be heated. Large-scale Alfvénic waves with amplitude $\approx 20\ \mathrm{km\,s^{-1}}$ and periods of 100 to 500 s have been observed in the transition region and corona by McIntosh et al.[1] and are energetic enough to power the quiet corona and fast solar winds. Magnetic reconnection may also play a part in heating the corona,[2] and can be observed as spatially compact explosive events (EEs) in the transition region and upper solar atmosphere.[3,4] These events contrast Alfvén waves with much shorter lifetimes (≈ 75 s) and Doppler velocities on the order of $100\ \mathrm{km\,s^{-1}}$ (see Ref. 5 and references therein). Imaging either of these events with a slit style spectrograph can be challenging, and is usually the result of a combination of fortuitous positioning of the spectrograph slit, rastering, and exposure timing.

The Multi-Order Solar EUV Spectrograph (MOSES)[5,6] is a sounding rocket-based snapshot imaging spectrograph. MOSES obtains high cadence (≈ 10 s) spectral and spatial information simultaneously over a $20' \times 10'$ field of view (FOV) by omitting the entrance slit usually associated with rastering-type spectrometers.[5] The high spatial resolution ($0.6''$ pixels) and large FOV of MOSES make it possible to capture a multitude of EEs and traveling wave phenomena within a single exposure. MOSES shares this characteristic with other ground based instruments, such as the computed tomography imaging spectrometer,[7] and the ground-based observations made by DeForest et al.[8] using the Advanced Stokes Polarimeter on the Dunn Solar Telescope at the National Solar Observatory. Much like these two instruments, the increased FOV and temporal resolution of MOSES come at a cost. While MOSES can easily obtain cotemporal spectral and spatial information over a large FOV, disentangling the overlapping spectral and spatial information in the MOSES dispersed images presents an ill-posed inversion problem.

The MOSES instrument utilizes a concave spherical diffraction grating to form images of $m = 0$, $+1$, and -1 diffraction orders on three 2048×1024 rear-illuminated CCDs. A schematic of the grating and imaging detectors is shown in Fig. 1. The top, center, and bottom detector planes in Fig. 1 image the $m = +1$, 0, and -1 spectral orders, respectively. The spatial axis is the same in all three spectral orders; however, the direction of the dispersion axis is reversed between the $m = \pm 1$ orders. The images formed in these two orders are not redundant. When imaging an object that has some spectral width, components that are redward of the instrument passband center (the letter "A" in Fig. 1) are shifted away from the $m = 0$ order CCD in the $m = \pm 1$ order images. Conversely, the blueward components of the object ("B" in Fig. 1) are shifted toward the $m = 0$ order CCD. There is no dispersion in the $m = 0$ order images; intensity in this order is simply a function of position integrated over the instrument passband. Multilayer coatings and thin film filters limit the instrument passband to a few spectral lines, the brightest of which is the Lyman alpha transition of He II at 30.4 nm. More information about instrument specifics can be found in Ref. 5.

*Address all correspondence to: Hans T. Courrier, E-mail: hans.courrier@montana.edu

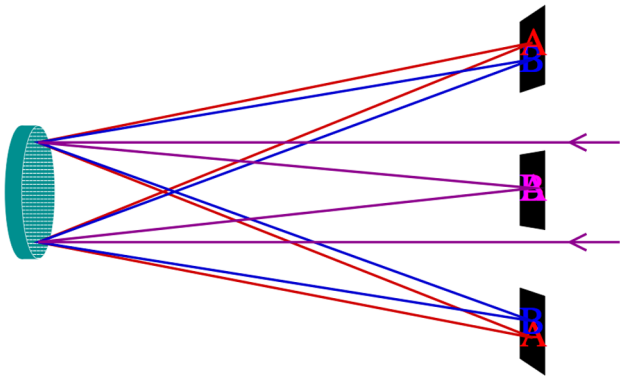

Fig. 1 Schematic diagram of the MOSES instrument. Incident light on the right forms an undispersed image on the central $m = 0$ CCD. Dispersed images are formed on the outboard $m = \pm 1$ CCDs.

Any pair of MOSES spectral orders contains information about Doppler shifts.[6] Fox et al.[9] proposed a pair of inversion techniques to solve the ill-posed problem of obtaining spectra for each pixel in a MOSES image. We propose a solution to a better posed problem; estimating just the Doppler shift from the strong He II line. Most of the solar emission within the instrument passband comes from this emission line. Doppler shifts are estimated by cross correlating corresponding patches of two simultaneous images to determine a local shift vector. The shift vector component parallel to the image dispersion direction then corresponds to the Doppler shift. This method is based on a stereoscopic inversion method described by DeForest et al.[8] for ground-based magnetography. The Fourier local correlation tracking (FLCT)[10] routine is employed as a fast and efficient means of performing the cross correlation and generating subsequent per pixel vector displacement fields for image pairs. There are two advantages to performing the inversion with local correlation tracking: (1) correlation is not affected by differing background levels in image pairs and (2) the method can track intensity in the dispersed and nondispersed axis of the images, allowing some compensation for differing aberration among image orders. In Sec. 2, we prepare a synthetic dataset that simulates MOSES flight data. We use this synthetic data to characterize the spatial and spectral response of the FLCT method in the context of a MOSES such as dataset, paying particular attention to how differing point spread functions (PSF) in the three spectral orders influence FLCT-derived Doppler shifts. We then use the results of Sec. 2 and FLCT to generate Dopplergrams of MOSES data collected during the February 2006 flight[6] in Sec. 3.

2 Methodology

In this section, we demonstrate how we use FLCT to perform the stereoscopic inversion between image pairs of the MOSES instrument. MOSES has three diffraction orders that are imaged simultaneously. This results in three independent image pairs for each exposure; $m = 0, +1$, $m = 0, -1$, and $m = +1, -1$. The inversion process can be described by three high-level operations: (1) FLCT determines displacement vectors for each pixel in an image pair, (2) the displacement vector array is converted into a line-of-sight (LOS) velocity array using the known instrument dispersion, and (3) "Dopplergrams" are created by overlaying the color-coded LOS velocities onto the $m = 0$ image. In Sec. 2.1, we determine the best FLCT parameters to reconstruct the Doppler velocity from MOSES data, and in Sec. 2.2, we investigate artifacts that result from instrument aberration and the FLCT-based inversion method.

2.1 *FLCT Parameters*

FLCT was designed to solve the "optical flow" problem[10] by finding a two-dimensional (2-D) flow field between two images taken at different times that results in the best reproduction of the second image when applied to the scalar field of the first. Pursuant to its originally intended purpose, FLCT has five adjustable parameters: (1) amount of time between input images, (2) unit of length of a single pixel, (3) optional threshold parameter to skip flow calculation for pixels based on input image intensities, (4) optional low pass filtering parameter applied in the FFT domain, and (5) characteristic width, σ, of a Gaussian windowing function applied to the input images. To output displacement vectors in pixels from FLCT, we set the ratio of the first two input arguments equal to unity. The optional threshold and low pass filtering parameters are not used. In this section, we discuss how we threshold FLCT output and choose the windowing parameter σ to provide the best stereoscopic inversion of MOSES data.

We choose to threshold FLCT output based on the MOSES $m = 0$ order image intensity for two reasons; (1) it places the FLCT-derived displacement vectors (Doppler shifts) over the $m = 0$ order image, rather than the abstracted spectrally "smeared" images produced by the $m = \pm 1$ orders, (2) as we explain below, FLCT tends to shift the velocity field when comparing $m = 0$ to $m = \pm 1$; thresholding using $m = 0$ intensity minimizes this effect. The zero-order image is the natural location for the LOS velocity, as this is where the spectral signal originates from. The shifted velocity field is presented in

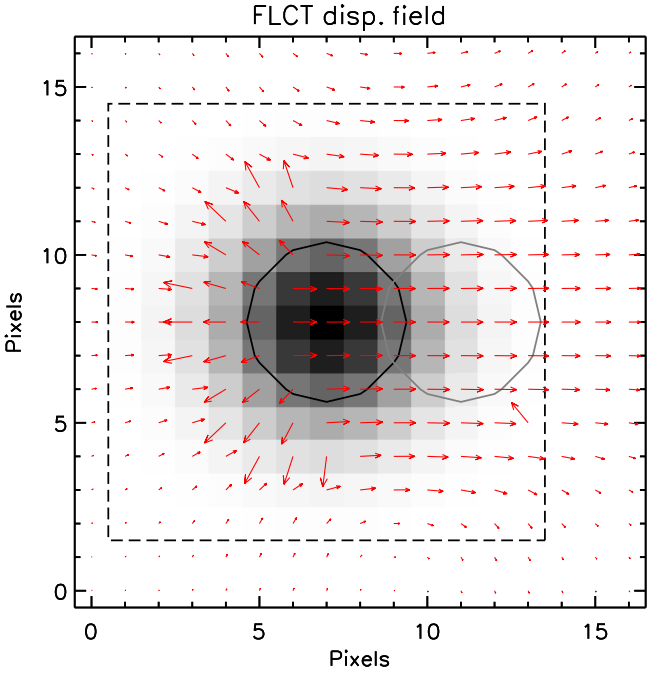

Fig. 2 FLCT-generated displacement vectors for a Gaussian that has been shifted four pixels to the right. The black contour is drawn at half maximum intensity. The gray contour marks the same and identifies the location of the shifted image. The dashed box marks 2σ for the FLCT windowing function ($\sigma = 3$), centered over the unshifted image; correlations outside of this box are considered unlikely. Displacement vectors are scaled to fit within one pixel.

Fig. 2, where FLCT has generated displacement vectors between two images of identical Gaussians ($\sigma = 2$ pixels) using a larger windowing function with $\sigma = 3$. An exaggerated displacement field is created by shifting one image four pixels horizontally with respect to the other. The dashed box centered over the left Gaussian marks the nominal correlation window size of 2σ. Although correlations are possible outside of this box, the purpose of the windowing function is to discourage correlations for comparatively large displacements. In Fig. 2, the displacement vectors are shifted to the right side of this box, to a point in between the two images, rather than over the left Gaussian. Thresholding Dopplergrams generated from the two outboard order images based on the zero-order intensity helps compensate for this offset of the Doppler velocities.

The optimal value of σ is largely dependent on the size scales present in our images.[8,10] MOSES images the solar transition region, which is highly dynamic. Small compact EEs (spatial size on the order of a few MOSES pixels) are associated with Doppler shifts of tens to hundreds of km s^{-1}.[6,11] In general smaller values of σ result in finer resolution in the displacement field, whereas larger values are better suited to reproducing larger shifts and reduce artifacts due to the differing size of the PSF for each image order. One major limitation of FLCT (and all local correlation techniques) is that spatial resolution of the extracted Doppler shift is affected by the correlation window size.[7,8] This effect is illustrated by the dashed box in Fig. 2, which marks where the Gaussian windowing function drops below four orders of magnitude for $\sigma = 3$. There must be sufficient features contained within this box for FLCT to derive a displacement vector, as the windowing function makes correlations increasingly unlikely for features that are located further away. Fortunately the solar transition region is finely structured, and acknowledging this limitation, we use knowledge of the MOSES instrument aberration for each image order to set a lower limit for σ.

Figures 3(a)–3(c) show 2-D estimates of the MOSES PSFs for each image order, estimated in Ref. 12. A contour is drawn at half maximum intensity, which indicates the size and shape of each PSF. As seen in Fig. 3, the three PSFs extend differently over several pixels along the horizontal (dispersed) and vertical (nondispersed) axes. Figures 3(d)–3(f) show line spread functions (LSFs) for the dispersed axis of each image order, obtained by summing over the vertical axis of the corresponding 2-D PSF. The width of each LSF is estimated by a least squares Gaussian fit. Modulation transfer functions (MTFs) derived from the LSFs of Fig. 3 are plotted in Fig. 4. MTFs for normalized Gaussian functions of $\sigma = 2$ and 3 are overplotted in dashed lines. Both Figs. 3 and 4 highlight the differences in imaging quality of the three MOSES image orders.

The disparity in aberration between image orders is a primary consideration in our selection of 2-D FLCT as an inversion method. The difference in aberration between image orders causes intensity information, and thereby spectral information, to be mapped differently into each of the MOSES image orders. Vertical displacement between image pairs is wholly a result of instrument aberration, since this axis is not dispersed. On the

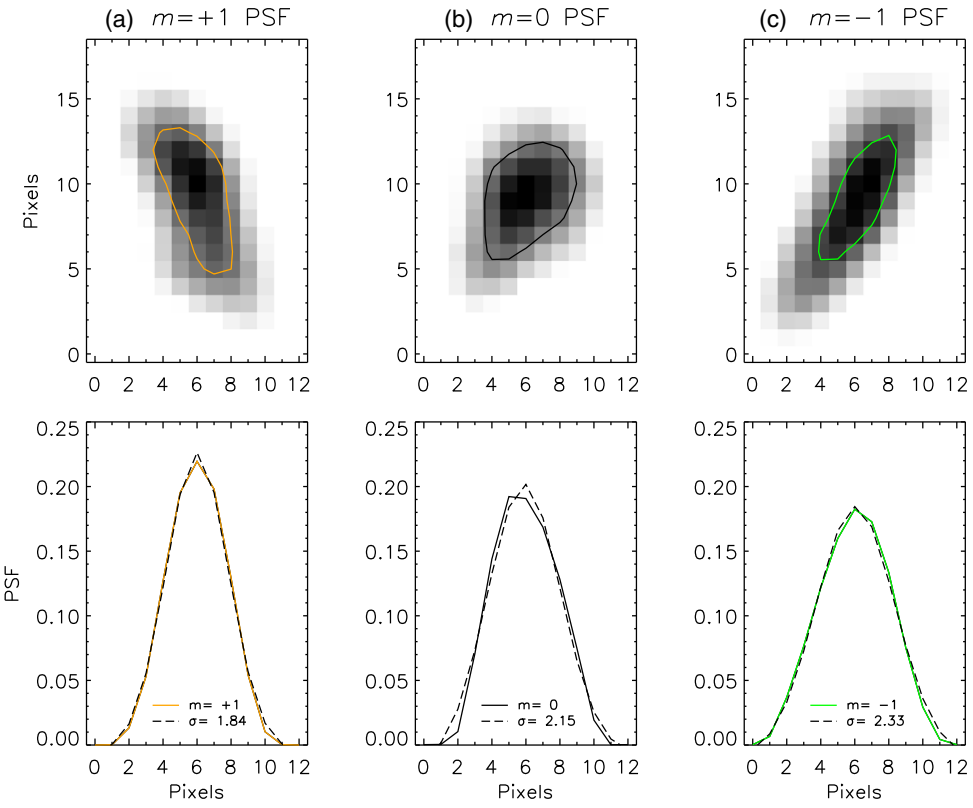

Fig. 3 Estimates of the MOSES $m = +1$, 0, and −1, image order PSFs in columns (a), (b), and (c), respectively. The contour is drawn at half maximum intensity for each PSF image in the top row. In the bottom row, LSFs are formed by summing along the vertical axis of the PSF image directly above. A Gaussian with characteristic width σ is fit to each LSF in the bottom panels, and overplotted as dashed curves.

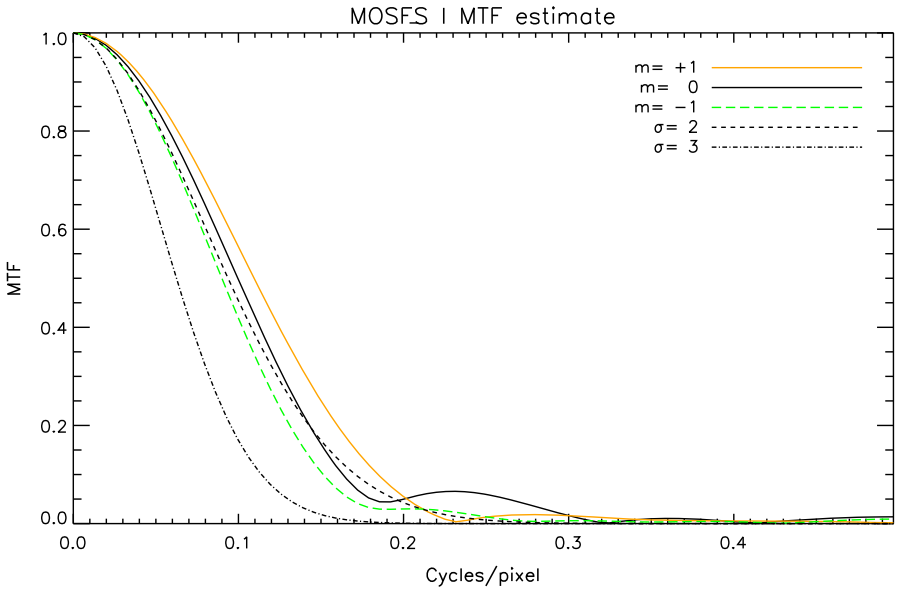

Fig. 4 MTFs for each of the MOSES image orders, derived from the LSFs of Fig. 3. Overplotted in dashed and dash-dot curves are MTFs of FLCT Gaussian windowing functions with $\sigma = 2$ and 3.

other hand, horizontal displacement is due to some combination of the spectral content of the signal and instrument aberration. We include the vertical component of displacement, so signal that has moved in this direction due to PSF differences can be identified and tracked. This is explained by the FLCT-generated displacement vectors for two simplified cases in Fig. 5.

In Figs. 5(a)–5(c), we estimate the instrument response to a point source with singular spectral content. In this case the point source is not shifted in the $m = \pm 1$ orders, so that the centroids of the PSF for each image order are colocated. In Figs. 5(a) and 5(b), FLCT draws displacement vectors from the $m = 0$ to $m = +1$ and -1 image orders, respectively, whereas the vectors are drawn from the $m = +1$ to $m = -1$ image order in Fig. 5(c). In these three panels, the horizontal displacement vectors are near zero where the PSFs overlap in each image pair. Artificial displacement vectors appear where one PSF extends beyond the other in each image pair; we investigate

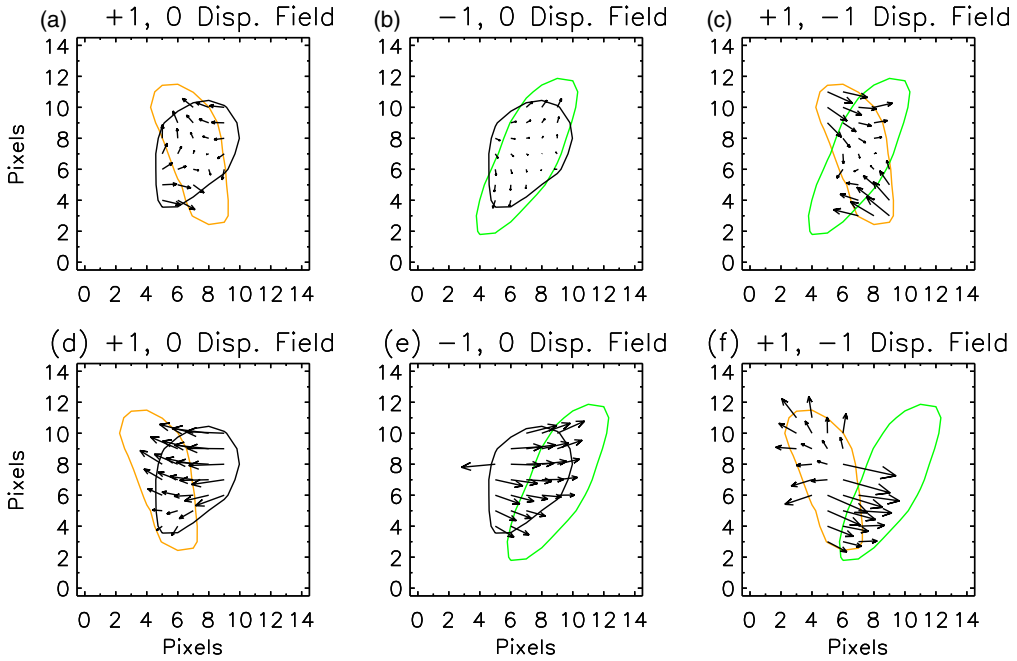

Fig. 5 FLCT-generated displacement vectors for a point source based on the PSF estimates of Fig. 3. Panels (a)–(c),the signal is monospectral. Panels (d)and (e), dispersion is added by means of a two pixel redward shift in the $m = \pm 1$ orders. This appears as a four pixel shift in (f) due to the symmetry of the instrument.

this in greater detail in Sec. 2.2. A window size of $\sigma = 3$ was used to generate the displacement vectors in all panels, based on the MTFs from Fig. 4. Since FLCT finds a corresponding point in the $m = \pm 1$ for every point in the $m = 0$ PSF in Fig. 5, and similarly for the $m = +1$ to $m = -1$ in Fig. 5(c), we assert that $\sigma = 3$ is sufficiently large to resolve this case.

In Figs. 5(d)–5(f), FLCT generates displacement vectors for a point source with some known spectral content. Each of these three panels is similar to the one above; however, a 58 km s^{-1} red shift has been simulated by shifting the $m = +1$ PSF leftward two pixels in Fig. 5(d) and the $m = -1$ PSF rightward by the same amount in Fig. 5(e). This appears as a four-pixel

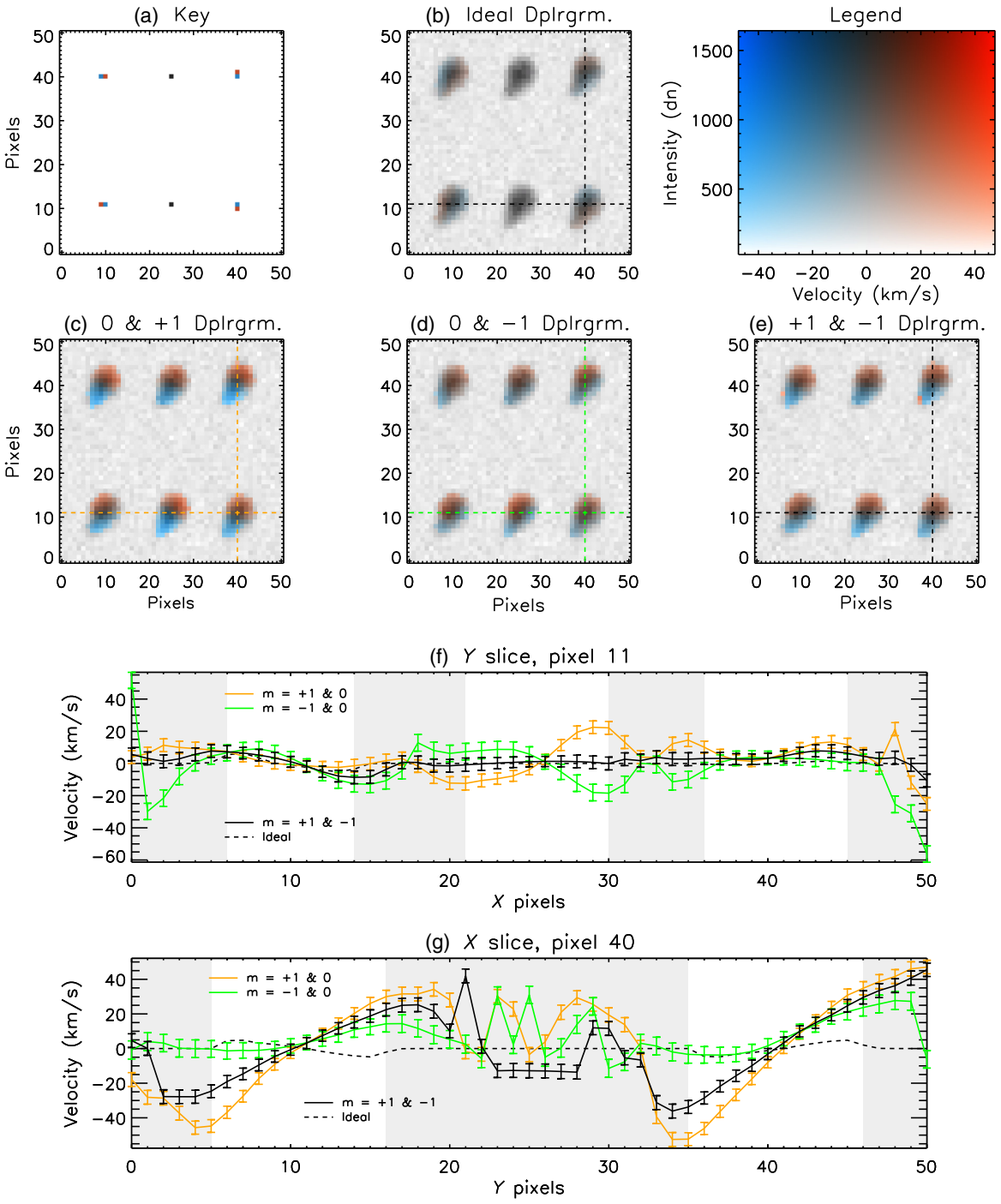

Fig. 6 Dopplergrams of synthetic images that mimic the MOSES instrument response to spatially unresolved point sources. The color indicates line shift in km s^{-1} while color saturation shows intensity. Panel (a) is the original input image, (b) is the expected instrument response. Panels (c), (d), and (e) are the inversion results for each image pair. Horizontal and vertical cuts of each Dopplergram are [indicated by dashed lines in panels (b) to (e)] plotted with error bars in panels (f) and (g), respectively. Gray region plots (f) and (g) indicate where Doppler velocities have been thresholded out of the Dopplergrams. Inversion results are dominated by systematic errors from instrument aberration (discussed in the previous section text) in this case where the point sources are not sufficiently resolved. (A color version of this figure is available in the online journal.)

displacement between PSF centroids in Fig. 5(f) due to the symmetry of the instrument. This two pixel displacement is well reproduced over the whole of the $m = 0$ PSF in Figs. 5(d) and 5(e), albeit with some errors in the nonoverlapping portions resulting from the differing PSF shapes noted earlier. The window size of $\sigma = 3$ remains sufficient to resolve this case for the image pairs in these two panels. In Fig. 5(f), FLCT has failed to correlate the upper portion of the $m = +1$ to $m = -1$ PSF. This is due in part to the elongated form and differing orientation of the PSFs as well as the increased displacement for a given Doppler shift for this image pair. Experimentation has shown that $\sigma = 5$ is a sufficiently large window size to map all of the intensity of the $m = +1$ PSF into the $m = -1$ PSF.

From these two cases, we conclude that setting the FLCT window parameter $\sigma = 3$ for the $m = 0, +1$ and $m = 0, -1$ image pairs and $\sigma = 5$ for the $m = +1, -1$ provides the optimal resolution for our inversion method.

2.2 *Inverting Synthetic Data*

To investigate how the FLCT-based inversion method recovers Doppler information from closely spaced sources, synthetic images that simulate the basic structure of compact and dynamic

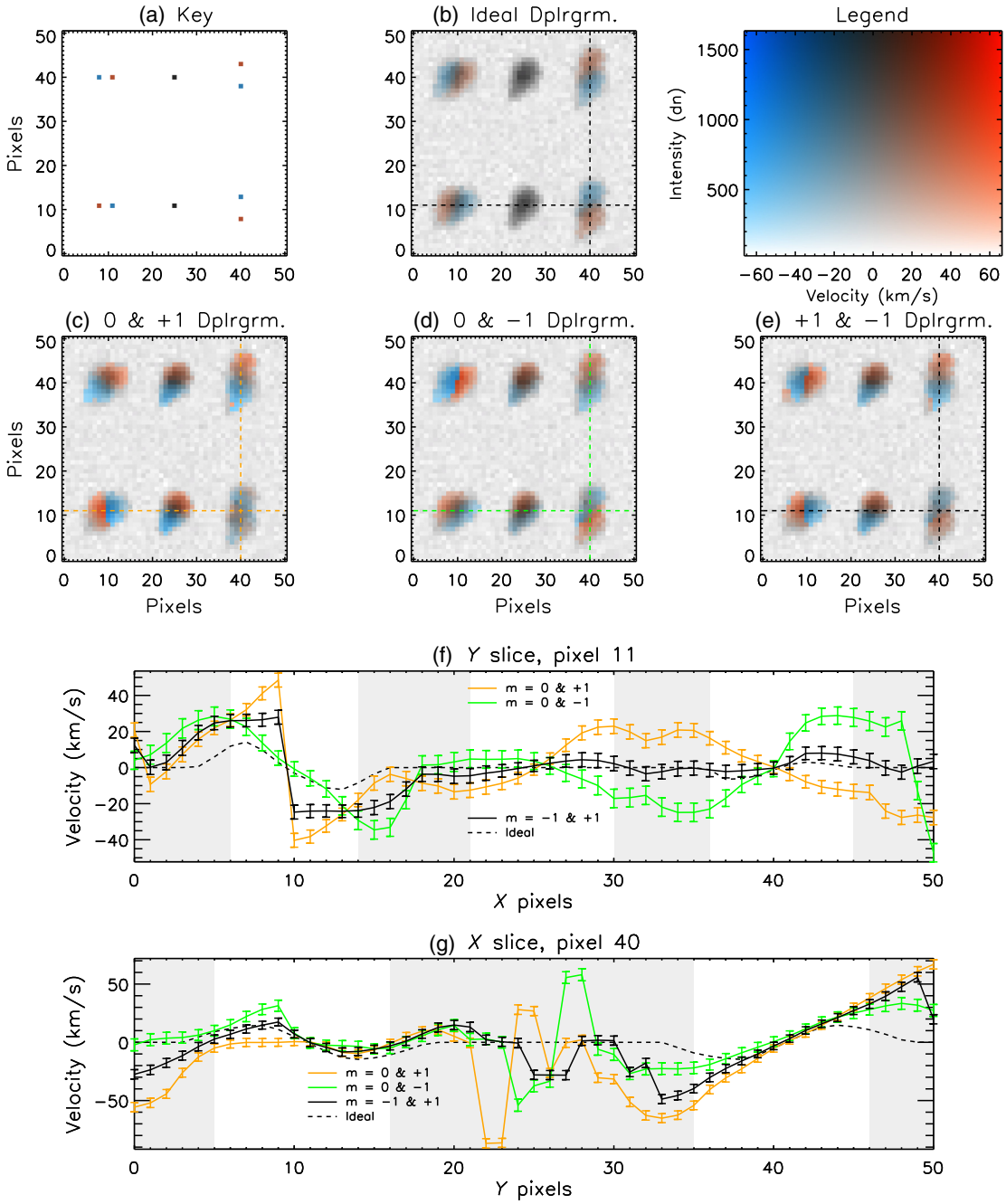

Fig. 7 Dopplergrams with increased spatial separation between spectral point sources. Panel layout is the same as Fig. 6; the original input image is shown in panel (a). Artifacts contribute to the under- and over-estimation of Doppler velocity in panels (c), (d), and (e), compared to (b), see text for details. (A color version of this figure is available in the online journal.)

events observed by MOSES were generated and analyzed. Two test cases are considered in Figs. 6(a) and 7(a); an unresolved and marginally resolved case, respectively. For both cases, the synthetic images consist of adjacent red, blue, and unshifted point sources. Point sources with Doppler shifts are colored blue or red to indicate direction, whereas the magnitude of the shift is 29 km s^{-1} for either direction in accordance with the legends in Figs. 6 and 7. In both Figs. 6(a) and 7(a), the point source located at (100, 85) has zero spectral linewidth, whereas the point source at (100, 100) has a linewidth of 29 km s^{-1}. These two test cases help to visualize the combined resolution limits of the imaging system and inversion method.

To mimic the MOSES instrument response for each image order, the synthetic images are first convolved with the appropriate PSF estimate from Fig. 3. Poisson noise is then added to each image, resulting in an approximation to compact, dim events observed throughout the FOV of MOSES. The signal to background for the $m = 0$ synthetic images is ~2.9, set in a background with mean of 424 counts. FLCT is then used to generate displacement vectors for each of the $m = 0, +1$, $m = 0, -1$, and $m = +1, -1$ image order pairs.

Dopplergrams from each of the image pairs are shown in Figs. 6(c)–6(e) and 7(c)–7(e). The component of the FLCT-derived displacement vectors parallel to the dispersion axis is converted to LOS velocity by multiplication with the instrument dispersion. The magnitude of the MOSES dispersion is 29 km s^{-1} per pixel for the $m = 0, +1$ and $m = 0, -1$ image pairs and 14.5 km s^{-1} per pixel for the $m = +1, -1$ image pair. The factor of two in difference in dispersion is due to the antisymmetry of dispersion of the $m = \pm 1$ image orders noted earlier. Dopplergrams are created by overlaying color-coded LOS velocities from each image pair on the $m = 0$ order image. In Figs. 6 and 7, the Dopplergrams are thresholded by binning the $m = 0$ order image counts into halves and ignoring those velocities corresponding to the dimmest half for clarity. Figures 6(f) and 6(g) and 7(f) and 7(g) show horizontal and vertical cuts through Dopplergrams (b)–(e). The gray background in these two plots indicates where Doppler velocity has been thresholded in the corresponding Dopplergrams. Nonthresholded Doppler velocities are shown in these regions to help characterize systematic errors in the inversion. Error bars indicate estimated uncertainty in Doppler velocity due to random intensity errors in the data, derived in Appendix A.

An additional Dopplergram is shown in Figs. 6(b) and 7(b). These Dopplergrams present the expected distribution of Doppler velocity information of the synthetic images after convolution with the $m = 0$ order PSF. The velocity field displayed on the $m = 0$ order image, $v'(x, y)$, is derived from the known velocity field, $v(x, y)$, of the synthetic images by

$$v'(x,y) = \frac{I(x,y)v(x,y) * \kappa}{I(x,y) * \kappa}, \quad (1)$$

where $I(x, y)$ is the intensity of the $m = 0$ order image in counts, κ is the $m = 0$ order PSF estimate, and * is the convolution operator. These "ideal" Dopplergrams illustrate how the Doppler information encoded into our synthetic images is distributed in the $m = 0$ order images.

Contrasting Doppler shifts in sources separated by only one pixel will not be resolved using FLCT with $\sigma = 3$ or $\sigma = 5$ window. This is illustrated in Figs. 6(c)–6(e), where the inversion is dominated by spurious Doppler shifts resulting from instrument aberration for all three image pairs. These artifacts appear as red shifts near the top of the reimaged point source, and blue shifts near the bottom, in Figs. 6(c)–6(e). For each of the three image pairs, the inversion returns similar results for all point sources regardless of their spectral content. Comparing Figs. 6(c)–6(e) to the ideal Dopplergram in Fig. 6(b), there is little correlation in Doppler velocity except where the orientation of point sources in Fig. 6(a) tends to match the orientation of the inversion artifacts. In Fig. 6(f) there is some correlation with true Doppler velocity near pixel 10, where systematic errors from the PSFs align well with the Doppler shifted point sources in Fig. 6(a), however the inversion returns spurious shifts for the other two features. This is most notable in Fig. 6(f), where the extracted Doppler shift is nearly identical for the features located at pixels 10 and 40, despite the inverted Doppler velocities shown in Fig. 6(a). For this case, where the spectral point sources are not well separated, the true Doppler shifts are overwhelmed by systematic error in the inversion.

The inversion method returns more favorable results when the separation between spectral point sources is increased. This is illustrated in Fig. 7(a) where the horizontal separation between red and blue shifted point sources is increased to three pixels horizontally and five pixels vertically. This is still below the spatial resolution indicated by the MTFs in Fig. 4; however, the additional spectral information allows us to resolve the point sources in Fig. 7(a) in most cases.

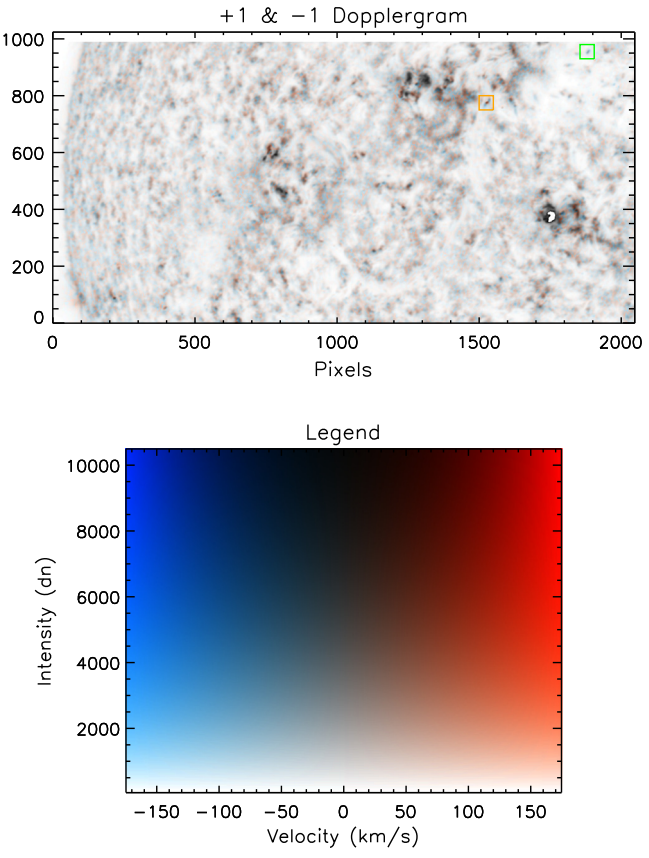

Fig. 8 Top panel, FLCT-generated dopplergram of a MOSES exposure from the $m = +1$ and −1 order images. White pixels are bad or missing data. Orange and green boxed areas are shown in greater detail in Figs. 9 and 10, respectively. Bottom panel, Doppler velocity and intensity legend for the dopplergram above. (A color version of this figure is available in the online journal.)

Comparing each of Figs. 7(c)–7(e) to 7(a), the basic structure of Fig. 7(a) is well reproduced by the inversion of each of the three image pairs. Comparing these same three panels with Fig. 7(b) shows that the inversion method reproduces the expected distribution of Doppler velocities but overestimates the magnitudes. This overestimation of Doppler magnitude is attributed to the artifacts that result from differing instrument aberration pointed out in Fig. 6.

In Fig. 7(f), the Doppler field offset discussed in Sec. 2.1 is evident near pixel 10. For the $m = 0, +1$ cut, the peak Doppler velocities occur near pixels 9 and 10, whereas lower peak velocities are reported by the $m = 0, -1$ cut at pixels 5 and 15, respectively. The Doppler field offset tends to smear the recovered Doppler signals together in the $m = 0, -1$ cut near pixel 10, resulting in a softening of the transition from red to blue shift. The inverse is true for the $m = 0, +1$ cut, as the recovered velocity field is smeared away from the transition area. The $m = -1, +1$ cut has a smoother response and the recovered signal tends toward the average of the other two cuts near pixel 10.

The $m = 0, +1$ image pair does not resolve the Doppler velocities for the feature centered at pixel (40, 11) in Fig. 7(a) and pixel 10 in Fig. 7(g). This is because the orientation of the point sources in Fig. 7 leads to an unfavorable configuration in

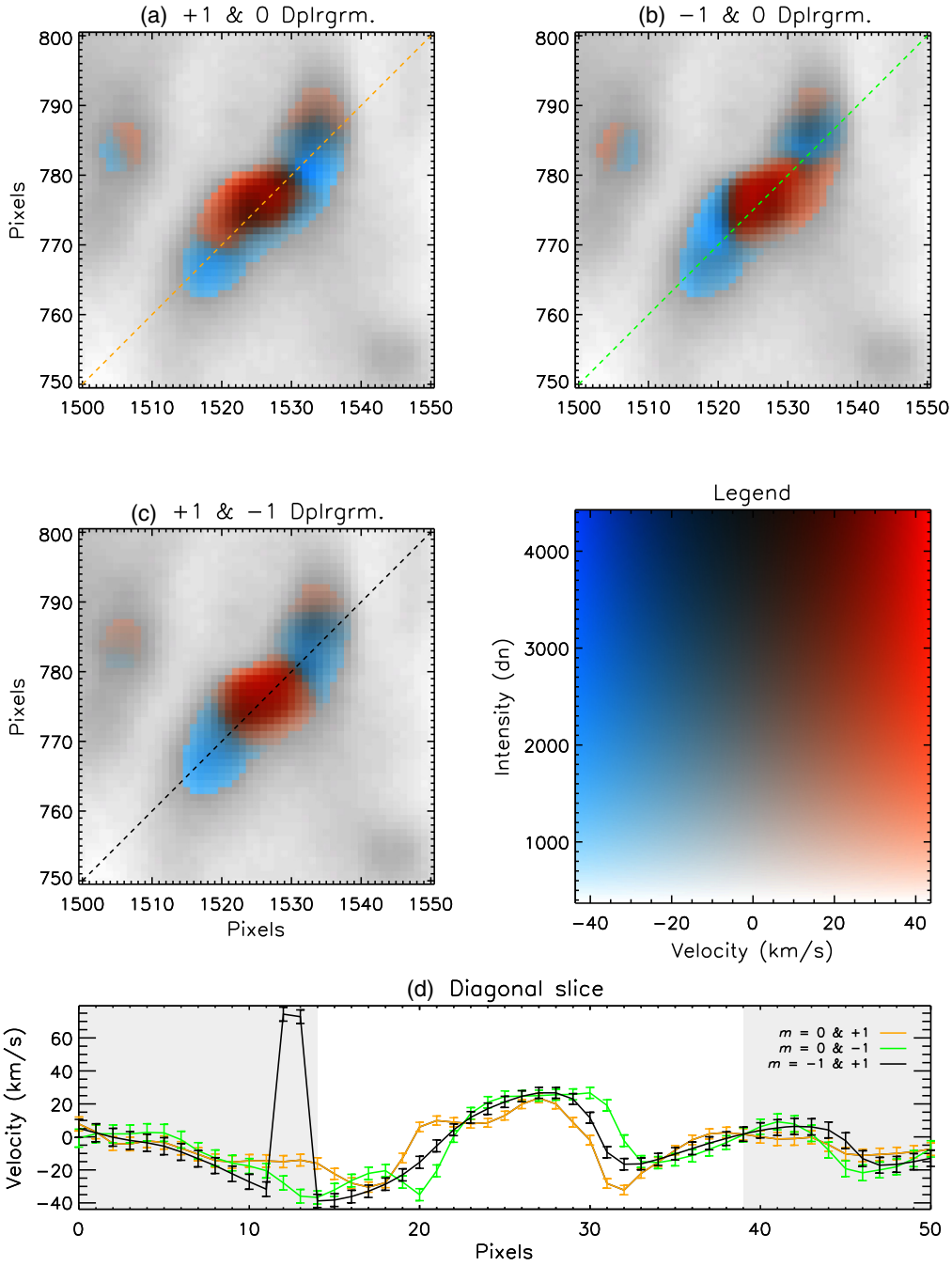

Fig. 9 Dopplergrams of a compact bidirectional explosive event observed by MOSES (a) +1 & 0, (b) -1 & 0, and (c) ±1 image orders. Diagonal cuts through the dopplergrams [panels (a)–(c), dashed lines] are plotted in panel (d). The differing location in each panel of the red shifted core of this event is an artifact of the inversion method, discussed in Sec. 2. (A color version of this figure is available in the online journal.)

the $m = +1$ image. In this case convolution with the $m = -1$ PSF causes the point sources to nearly overlap in the y-axis in this order, causing this feature to look nearly identical in the $m = 0$ and $m = -1$ orders. For this particular orientation of point sources, the y-axis resolution of the PSFs is the limiting factor. We note that the Doppler shifts of the opposite feature [pixel (40, 40) in Dopplergrams and Fig. 7(f), pixel 40] is well resolved, as the alignment of PSFs is more favorable for this feature.

Despite these shortcomings, Fig. 7 shows that FLCT is able to at least qualitatively reproduce Doppler shifts near the resolution limit for two images with differing PSFs. Moreover, sources separated by three pixels are resolved even when a $\sigma = 5$ FLCT window is used (e.g., Fig. 7). In most cases, the inversion method reproduces the general structure of the point sources (i.e., finding the correct sign of Doppler shift); however, systematic errors tend to under- or over-estimate the magnitude of the Doppler shifts.

3 Inverting MOSES Data

In this section, we apply FLCT Doppler estimation to representative images and features from solar observations obtained with MOSES. The MOSES instrument was launched February 8,

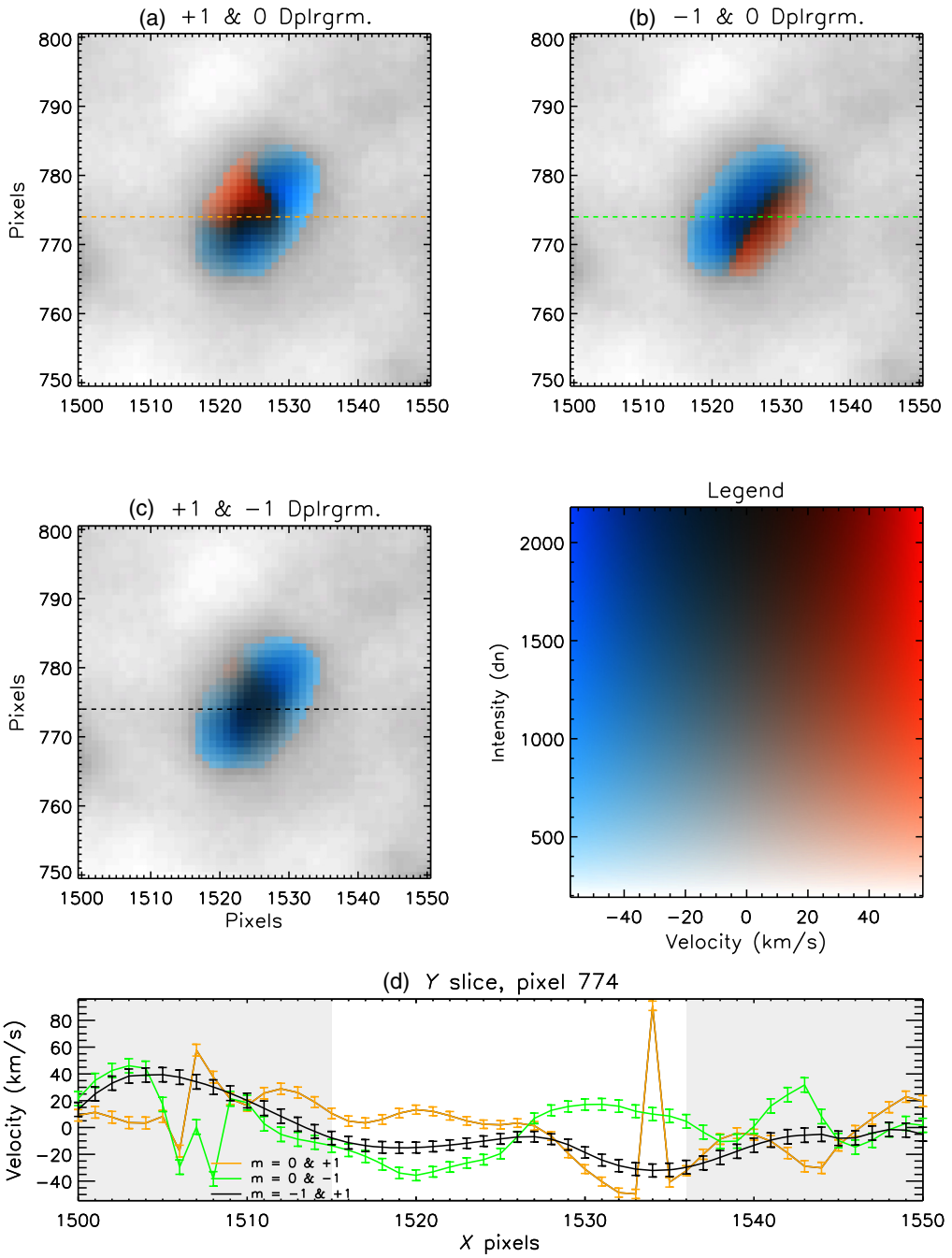

Fig. 10 Compact explosive event observed by MOSES; panel layout is the same as Fig. 9. Offset red shifts in panels (a) and (b) may indicate this event has a redshifted core. This red shift is not resolved in panel (c). See text for details. Horizontal cuts through the dopplergrams [panels (a)–(c), dashed lines] are plotted in panel (d). (A color version of this figure is available in the online journal.)

2006 from White Sands Missile Range, New Mexico. Over the course of ~5 min, 27 exposures were taken above 160 km. Data from this flight have been dark subtracted, the $m = \pm 1$ order images coaligned to the $m = 0$ order, and optical distortion removed from all images. Intensities are in units of data numbers (DN) per second. Exposures are normalized so that each image has the same mean DN s^{-1} as the exposure with least atmospheric absorption, the 14th exposure.[13] We generate Dopplergrams over the entire instrument FOV for each set of exposures in this image set guided by the results of Sec. 2. A value of $\sigma = 3$ is used for the $m = 0, +1$ and $m = 0, -1$ image pairs, whereas $\sigma = 5$ for the $m = +1, -1$ image pair.

A Dopplergram generated from the $m = -1$ and 0 orders of the 24th exposure is shown in Fig. 8. In this exposure, the orange boxed feature in Fig. 8 is fully developed and has also been analyzed in Refs. 6 and 13. The color map is scaled to ± 150 km s^{-1} as the majority of Doppler velocities fall within this range. Groups of white pixels in the FOV and the band of white pixels across the left side and top of the image are a result of bad, missing, or saturated pixels in one or more image orders. The image in Fig. 8 exemplifies the cotemporal spectral and spatial data the MOSES instrument collects over a large FOV within a single exposure. Several small, isolated features that show characteristics similar to transition region EEs[6,11] appear in these exposures. Two of these features are shown in the orange and green boxed areas of Fig. 8, and in greater detail in Figs. 9 and 10, respectively.

The feature shown in Fig. 9 is the same EE analyzed in Ref. 6. Our analysis produces similar structure, with the core of the feature largely red shifted, becoming blue shifted in the lower wing and red shifted near the tip of the upper wing. Unlike the analysis in Ref. 6, we resolve the upper wing as mostly blue shifted, only becoming red shifted toward the tip. We also find the core of the feature to be red shifted. The differing offset of this red shift in Figs. 9(a) and 9(b) is due to the Doppler field shift, described in Sec. 2.1. Based on our analysis in previous sections, the true position of this red shift is more closely reproduced in Fig. 9(c). Blue shifts are also affected by the Doppler field offset, leading to a softening of the transition from red to blue in the $m = 0, -1$ and $m = 0, +1$ cuts of Fig. 9(d) near pixel 32 and 19, respectively. Despite these systematic errors, this event appears well resolved by the inversion method as all three Dopplergrams report similar velocities and structure in Fig. 9(d).

The feature shown in Fig. 10 has some hidden complexity. This appears to be an entirely blue shifted event in the $m = -1, +1$ Dopplergram; however, a red shift near the center of the feature is registered in both Figs. 10(a) and 10(b). This indicates that this feature is only partially resolved by our inversion method and may be a compact version of the event in Fig. 9, with a red shifted core and blue shifted wings extending to the north and south. The Doppler field offset spreads the red and blue shifts away from the core of the event in Figs. 10(a) and 10(b) [similar to Figs. 10(a) and 10(b) of the Fig. 9], and PSF artifacts may contribute to overestimation of the peak red and blue shifts. The red shift near center is not resolved in Fig. 10(c) from a combination of unfavorable PSF alignment and the larger correlation window size in this Dopplergram. The $m = 0, +1$ and $m = 0, -1$ velocity cuts in Fig. 10(d) show that the red shifts extend nearly to the core of the feature in each case, also indicating that a red shift may be buried in the core of this feature.

4 Discussion and Conclusions

The MOSES instrument is designed to provide simultaneous imaging and spectroscopic information in a single snapshot over a wide FOV. To accomplish this, MOSES collects simultaneous EUV images in three spectral orders of a concave diffraction grating. Here we have demonstrated, on both synthetic and real data, the derivation of Dopplergrams from image pairs using local correlation tracking. Applications of FLCT to actual MOSES data in Sec. 3 show some promising results. Strong events such as those shown in Figs. 9 and 10 look broadly similar whether the Dopplergram is generated from the $m = 0, +1$, $m = 0, -1$, or $m = +1, -1$ order image pairs. Comparing the features of Fig. 10 to the synthetic images of Fig. 7, it is clear that resolving the Doppler shifts of adjacent features located within one PSF radius (~3 pixels) is near the limitations of our FLCT-based method. However, for a $\sigma = 3$ and even $\sigma = 5$ window, the spatial resolution of our Doppler maps is only modestly degraded in comparison with the original intensity maps [e.g., Fig. 7(d) in which Doppler shifts are resolved for sources three and five pixels apart]. Reference 8 employed a difference of image intensity integrals along the dispersion axis to capture the finest details. Before we can reach that level of detail with MOSES data, we will need to apply explicit PSF correction.[14] In Sec. 2, we show the origin of systematic errors that mainly affect poorly resolved structures. Some of these systematic errors are due to the differing PSFs of each image order. While the inversion method can compensate for some degree of disparity between PSFs of the image orders, and the three available Dopplergrams help identify these systematic errors, the method would be improved treating PSF errors in the data prior to analysis. A procedure that equalizes PSFs between image orders (e.g., the procedure under preparation in Ref. 14) could reduce or eliminate these systematic errors, and may be preferable to deconvolution of the PSF estimates.

It is also apparent from Sec. 2 that FLCT systematically shifts the locations of the Doppler shifts. This unfortunately hampers quantitative, pixel-by-pixel comparison of the Dopplergrams derived from the $m = 0, +1$ and $m = 0, -1$ image orders. It would be helpful to develop a similar algorithm that places the Doppler shifts (displacement vectors) at the source locations in the $m = 0$ order image, rather than between the $m = \pm 1$ and $m = 0$ order images. Once this shortcoming is addressed, we expect to be able to better assess and improve our Doppler shift estimates by comparing and perhaps combining results gained from different image order pairs.

Moving forward, our strategy will be (1) remove or reduce PSF contributions in the MOSES data, (2) develop a local correlation tracking algorithm that minimizes or eliminates the offset of the displacement field, and (3) apply this algorithm to both synthetic and real MOSES data, as we have done in this study.

Appendix A: Error Estimation

In this section, we estimate error in correlation between two images due to random intensity errors in the data. We begin by assuming we have two different 1-D Gaussian intensity distributions, $F(x)$ and $G(x)$, centered at the origin

$$F(x) = f(x) \pm \varepsilon_f = f_0 e^{\frac{-x^2}{2\sigma_f^2}} + E_f(x), \tag{2}$$

$$G(x) = g(x) \pm \varepsilon_g = g_0 e^{\frac{-x^2}{2\sigma_g^2}} + E_g(x), \tag{3}$$

Table 1 Error model parameters at 30.4 nm.

CCD	σ_m (pixel)	j (DN/photon)	σ_r^2 (DN)
$m=-1$	2.33	1.79	4.4
$m=0$	2.15	1.73	4.3
$m+1$	1.84	1.76	5.1

where x is position in pixels, f_o is intensity at $x=0$, σ_f is the characteristic width of the distribution, $E_f(x)$ is per pixel Gaussian distributed noise with mean zero and standard deviation ε_f, and similarly for Eq. (3). The correlation function is then written

$$H(x) = F(x) \otimes G(x) \approx \frac{\sqrt{2\pi} f_0 g_0 \sigma_f \sigma_g}{\sqrt{\sigma_f^2 + \sigma_g^2}} e^{\frac{-x^2}{2(\sigma_f^2+\sigma_g^2)}} + [f(x) \otimes E_g(x)] + [g(x) \otimes E_f(x)], \tag{4}$$

where $\otimes$ is the cross-correlation operator. Assuming the real intensity distributions contain sufficient background so that $E_f(x)$ and $E_g(x)$ vary only weakly with x, we write

$$f(x) \otimes E_g(x) \approx \varepsilon_g \sqrt{\int_{-\infty}^{\infty} f^2(x) dx} = f_0 \varepsilon_g \sqrt{\sigma_f} \pi^{\frac{1}{4}}, \tag{5}$$

$$g(x) \otimes E_f(x) \approx \varepsilon_f \sqrt{\int_{-\infty}^{\infty} g^2(x) dx} = g_0 \varepsilon_f \sqrt{\sigma_g} \pi^{\frac{1}{4}}. \tag{6}$$

The uncertainty in $H(x)$ is, therefore

$$\sigma_\otimes = \sqrt{\sqrt{\pi}\sigma_f (f_0 \varepsilon_g)^2 + \sqrt{\pi}\sigma_g (g_0 \varepsilon_f)^2}, \tag{7}$$

where Eq. (7) results from adding Eqs. (5) and (6) in quadrature. For small displacements of x (not accounting for errors in intensity), we Taylor expand the first term of Eq. (4) so that

$$h(x) \approx \frac{\sqrt{2\pi} f_0 g_0 \sigma_f \sigma_g}{\sqrt{\sigma_c^2 + \sigma_g^2}} \left[1 + \frac{-x^2}{2(\sigma_f^2 + \sigma_g^2)}\right]. \tag{8}$$

To find how the position of the maximum correlation, $h(0)$, varies with intensity fluctuations, we solve

$$h(0) - h(x) = \sigma_\otimes, \tag{9}$$

for x. The error in Doppler velocity from random intensity fluctuations, σ_d, is then x multiplied by the MOSES pixel dispersion (29 km s^{-1}) so that

$$\sigma_d = 29 \times \sqrt{\frac{\sqrt{2}(\sigma_f^2 + \sigma_g^2)^3}{f_0 g_0 \sigma_f \sigma_g}} \left[\frac{\sigma_f (f_0 \varepsilon_g)^2}{\sqrt{\pi}} + \frac{\sigma_g (g_0 \varepsilon_f)^2}{\sqrt{\pi}}\right]^{\frac{1}{4}}. \tag{10}$$

Values of σ_f and σ_g are estimated for each MOSES image order by the Gaussian fits in Fig. 3. For convenience, we list the characteristic width, σ_m, together with gain (j) and read noise (σ_r^2) determined in Ref. 15 in Table 1 for each of the MOSES CCDs. The value of ε_f is then

$$\varepsilon_f^2 = j f_0 + \sigma_r^2, \tag{11}$$

for each image order, and similarly for ε_g.

Acknowledgments

This work was supported by the NASA Heliophysics Sounding Rocket Program, Grant No. NNX14AK71G.

References

1. S. W. McIntosh et al., "Alfvénic waves with sufficient energy to power the quiet solar corona and fast solar wind," *Nature* **475**, 477–480 (2011).
2. D. W. Longcope and L. A. Tarr, "Relating magnetic reconnection to coronal heating," *Philos. Trans. R. Soc. A* **373**, 20140263 (2015).
3. K. Dere, "Explosive events, magnetic reconnection, and coronal heating," *Adv. Space Res.* **14**, 13–22 (1994).
4. K. P. Dere et al., "Explosive events and magnetic reconnection in the solar atmosphere," *J. Geophys. Res.* **96**, 9399–9407 (1991).
5. J. L. Fox, C. C. Kankelborg, and R. J. Thomas, "A transition region explosive event observed in He II with the MOSES sounding rocket," *Astrophys. J.* **719**, 1132–1143 (2010).
6. C. C. Kankelborg and R. J. Thomas, "Simultaneous imaging and spectroscopy of the solar atmosphere: advantages and challenges of a 3-order slitless spectrograph," *Proc. SPIE* **4498**, 16–26 (2001).
7. M. Descour and E. Dereniak, "Computed-tomography imaging spectrometer: experimental calibration and reconstruction results," *Appl. Opt.* **34**(22), 4817–4826 (1995).
8. C. Deforest et al., "Stereoscopic spectroscopy for efficient spectral imaging and magnetography," *Astrophys. J.* **616**, 600–616 (2004).
9. J. L. Fox, C. C. Kankelborg, and T. R. Metcalf, "Data inversion for the multi-order solar extreme-ultraviolet spectrograph," *Proc. SPIE* **5157**, 124–132 (2003).
10. G. H. Fisher and B. T. Welsch, "FLCT: a fast, efficient method for performing local correlation tracking," in *Subsurface and Atmospheric Influences on Solar Activity*, ASP Conference Series, R. Howe et al., Eds., Vol. **383**, pp. 373–380, Astronomical Society of the Pacific, San Francisco (2008).
11. K. P. Dere, J. D. F. Bartoe, and G. E. Brueckner, "Explosive events in the solar transition zone," *Sol. Phys.* **123**(1), 41–68 (1989).
12. T. Rust, Private Communication (2015).
13. J. L. Fox, "Snapshot imaging spectroscopy of the solar transition region: the multi-order solar EUV spectrograph (MOSES) sounding rocket mission," PhD Thesis, Montana State University, Bozeman, Montana (2011).
14. S. Atwood and C. Kankelborg, "A PSF equalization technique for the multi-order solar extreme ultraviolet spectrograph (MOSES)," *Proc. SPIE* **9643**, 96431R (2017).
15. T. L. Rust, "Explosive events in the quiet sun: extreme ultraviolet imaging spectroscopy instrumentation and observations," PhD Thesis, Montana State University, Bozeman, Montana (2017).

Hans T. Courrier is a PhD candidate in physics at Montana State University. He has been involved in two successful launches of the MOSES sounding rocket instrument and performed the detailed optical design analysis for a new rocket-borne instrument called ESIS. He is experienced in science operations and data analysis for the NASA IRIS Small Explorer mission. Hans looks forward to joining the Bozeman photonics industry in the spring of 2018.

Charles C. Kankelborg is a professor of physics at Montana State University in Bozeman, Montana. His research interests are observation and modeling of the solar corona and transition region, XUV instrumentation, and inverse problems. He is principal investigator of the MOSES and ESIS sounding rocket experiments, and coinvestigator on the NASA IRIS satellite mission. His honors include several teaching awards and a 2008 Presidential Early Career Award.